Nuclear Instruments and Methods in Physics Research A 659 (2011) 161–168

Contents lists available at SciVerse ScienceDirect

Nuclear Instruments and Methods in Physics Research A

journal homepage: www.elsevier.com/locate/nima

Scintillation-only based pulse shape discrimination for nuclear and electron recoils in liquid xenon

K. Ueshima [a,*], K. Abe [a], K. Hiraide [a], S. Hirano [a], Y. Kishimoto [a,b], K. Kobayashi [a], Y. Koshio [a], J. Liu [b], K. Martens [b], S. Moriyama [a,b], M. Nakahata [a,b], H. Nishiie [a], H. Ogawa [a], H. Sekiya [a], A. Shinozaki [a], Y. Suzuki [a,b], A. Takeda [a], M. Yamashita [a,b], K. Fujii [c], I. Murayama [c], S. Nakamura [c], K. Otsuka [b], Y. Takeuchi [d,b], Y. Fukuda [e], K. Nishijima [f], D. Motoki [f], Y. Itow [g], K. Masuda [g], Y. Nishitani [g], H. Uchida [g], S. Tasaka [h], H. Ohsumi [i], Y.D. Kim [j], Y.H. Kim [k], K.B. Lee [k], M.K. Lee [k], J.S. Lee [k]

[a] Kamioka Observatory, Institute for Cosmic Ray Research, The University of Tokyo, Kamioka, Hida, Gifu 506-1205, Japan
[b] Institute for the Physics and Mathematics of the Universe, The University of Tokyo, Kashiwa, Chiba 277-8582, Japan
[c] Department of Physics, Faculty of Engineering, Yokohama National University, Yokohama 240-8501, Japan
[d] Department of Physics, Kobe University, Kobe, Hyogo 657-8501, Japan
[e] Department of Physics, Miyagi University of Education, Sendai, Miyagi 980-0845, Japan
[f] Department of Physics, Tokai University, Hiratsuka, Kanagawa 259-1292, Japan
[g] Solar Terrestrial Environment Laboratory, Nagoya University, Nagoya, Aichi 464-8602, Japan
[h] Department of Physics, Gifu University, Gifu, Gifu 501-1193, Japan
[i] Faculty of Culture and Education, Saga University, Honjo, Saga 840-8502, Japan
[j] Department of Physics, Sejong University, Seoul 143-747, Korea
[k] Korea Research Institute of Standards and Science, Daejeon 305-340, Korea

The XMASS Collaboration

ARTICLE INFO

Article history:
Received 13 June 2011
Received in revised form
30 August 2011
Accepted 7 September 2011
Available online 17 September 2011

Keywords:
Scintillation
Liquid xenon
Pulse shape discrimination

ABSTRACT

In a dedicated test setup at the Kamioka Observatory we studied pulse shape discrimination (PSD) in liquid xenon (LXe) for dark matter searches in the absence of an externally applied electric field. PSD in LXe was based on the observation that scintillation light from electron events was emitted over a longer period of time than that of nuclear recoil events, and our method used a simple ratio of early to total scintillation light emission in a single scintillation event. Requiring an efficiency of 50% for nuclear recoil retention we reduced the electron background by a factor of $7.7 \pm 1.1(\text{stat}) \pm {}^{1.2}_{0.6}(\text{sys}) \times 10^{-2}$ at energies between 4.8 and 7.2 keV_{ee} and $7.7 \pm 2.8(\text{stat}) \pm {}^{2.5}_{2.8}(\text{sys}) \times 10^{-3}$ at energies between 9.6 and 12 keV_{ee} for a scintillation light yield of 20.9 photoelectrons/keV_{ee}. Further study was done by masking some of that light to reduce this yield to 4.6 photoelectrons/keV_{ee}. Under these conditions the same method results in an electron event reduction by a factor of $2.4 \pm 0.2(\text{stat}) \pm {}^{0.3}_{0.2}(\text{sys}) \times 10^{-1}$ for the lower of the energy regions above. We also observe that in contrast to nuclear recoils the fluctuations in our early to total ratio for electron events are larger than expected from statistical fluctuations.

1. Introduction

The results of various astronomical observations [1–5] show strong evidence for a large amount of dark matter in the universe. Weakly Interactive Massive Particles (WIMPs) are a dark matter candidate motivated in extensions of the theory of high energy particle physics [6]. Various dedicated WIMP dark matter search experiments are underway around the world [7–9]. The XMASS experiment, using liquid xenon (LXe) as a target for WIMP dark matter, was proposed in 2000 [10]. The construction of the 800 kg detector was finished in 2010.

The interaction of WIMP dark matter is expected to be observed as a nuclear recoil in a specific detector's target material, which in our case is LXe. The main backgrounds (BG) for such nuclear recoil events are electron events (from photoabsorption or Compton scattering of environmental gamma rays), nuclear recoils from the scattering of fast neutrons, and possibly alpha and beta decays in the detector medium itself. The aim of this study is to use the shape of scintillation light pulse in LXe to discriminate against electron events.

* Corresponding author.
E-mail address: ueshima@suketto.icrr.u-tokyo.ac.jp (K. Ueshima).

0168-9002/$ - see front matter © 2011 Published by Elsevier B.V.
doi:10.1016/j.nima.2011.09.011

The scintillation mechanism is classified into two processes depending on whether or not the process involves recombination [11].

(1) The process without recombination:

$$Xe^* + Xe \rightarrow Xe_2^*$$
$$Xe_2^* \rightarrow 2Xe + h\nu. \quad (1)$$

(2) The process with recombination:

$$Xe^+ + Xe \rightarrow Xe_2^+$$
$$Xe_2^+ + e^- \rightarrow Xe^{**} + Xe$$
$$Xe^{**} \rightarrow Xe^* + \text{heat}$$
$$Xe^* + Xe \rightarrow Xe_2^*$$
$$Xe_2^* \rightarrow 2Xe + h\nu. \quad (2)$$

Both processes lead to the formation of an exciton (Xe_2^*). The de-excitation has two components called singlet and triplet component. The singlet component is caused by a spin singlet state ($^1\Sigma_u^+$), and the triplet component is caused by a spin triplet state ($^3\Sigma_u^+$) [12].

The shape of the scintillation light pulse in LXe is determined by the lifetimes of the excited states, the time scale of electron–ion recombination, the timing resolution of the scintillation light detector, the time of flight in the detector, and the electronics employed to record the scintillation light. The convolution of all these components shapes the recorded scintillation light pulses.

Pulse shape measurements for 1 MeV electrons, α particles, and relativistic ions in LXe were reported [13]. In the case of α particles, two distinct lifetime components were observed. The lifetimes for singlet and triplet states were found to be approximately 4 ns and 22 ns respectively. In the case of electron events on the other hand, only one long component with 45 ns lifetime was observed.

This pulse shape difference is attributed to the influence of electron–ion recombination [14,15]. In the case of electron events, dE/dx is one order of magnitude smaller than in the case of a nuclear recoil [14,16], and the ensuing ionization is thus spread out over a larger volume. Therefore the recombination process of electron events takes longer than in the case of nuclear recoil events and dominates the pulse evolution. This hypothesis was confirmed by measurements in electric fields, as the slow component was not observed when an external electric field is applied. Under the influence of an external electric field recombination is suppressed as the electrons and ions are drifted apart, and the two components characteristic of high dE/dx events re-emerge. The pulse shape of electron events in an electric field of 4 kV/cm is very similar to that of nuclear recoils in zero electric field [12]. In this paper we aim to exploit the characteristically longer time constant of 45 ns observed for electron events in LXe at zero electric field.

To this end we examine pulse shape discrimination (PSD) in LXe at energies of less than 20 keV_{ee} (electron equivalent keV). This energy range is most relevant for dark matter searches. The average waveform of nuclear recoil and electron events was previously compared above 10 keV_{ee} [17]. But no event-by-event analysis was done. An event-by-event analysis was reported [18], but the scintillation light yield was one order of magnitude lower than for our setup. One other PSD study was performed in a dual phase detector [19]. A reduction factor for electron events of 0.2 by PSD alone was demonstrated at 5 keV_{ee} in that dual phase detector by limiting the electric field to 0.06 kV/cm.

Previous investigations [17–19] were done at scintillation light yields below 5 photoelectrons/keV_{ee} (p.e./keV_{ee}). Using two closely spaced photomultipliers (PMTs) of the kind also used in the XMASS experiment we measured a light yield of 20.9 p.e./keV_{ee}. The higher light yield we obtained will allow a more detailed study of PSD at energies as low as 5 keV_{ee}. Anticipating more limited light collection in real detectors we artificially reduced the photosensitive area in our experimental setup and repeated the measurements at an effective light yield of 4.6 p.e./keV_{ee}.

2. Detector setup

Our measurements were made in a dedicated setup shown in Fig. 1. Two 2 in. hexagonal PMTs (Hamamatsu R10789) facing each other from a distance of 60 mm are viewing the enclosed

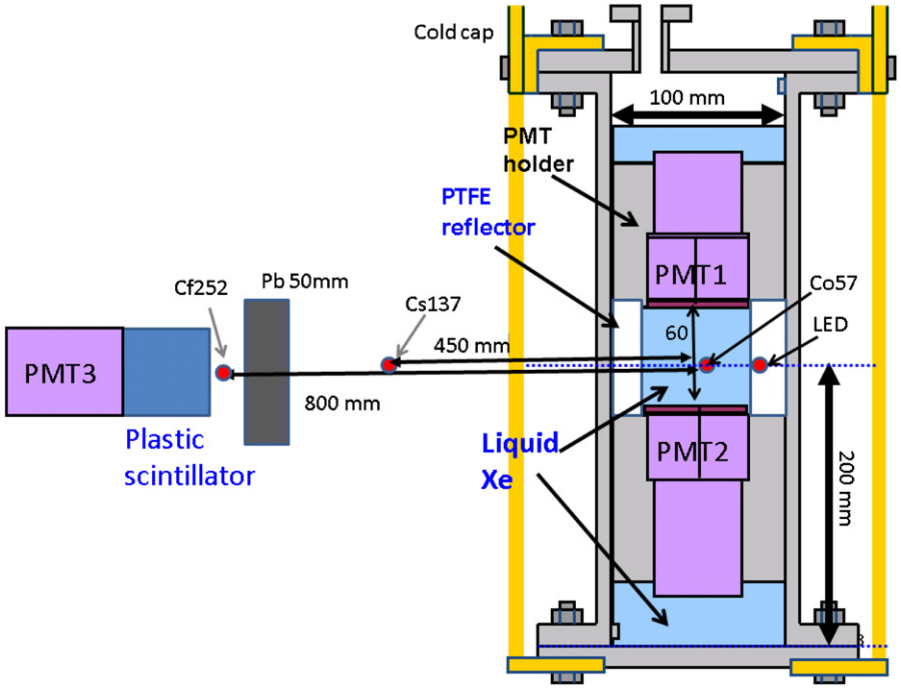

Fig. 1. A schematic view of the detector used in the PSD measurement.

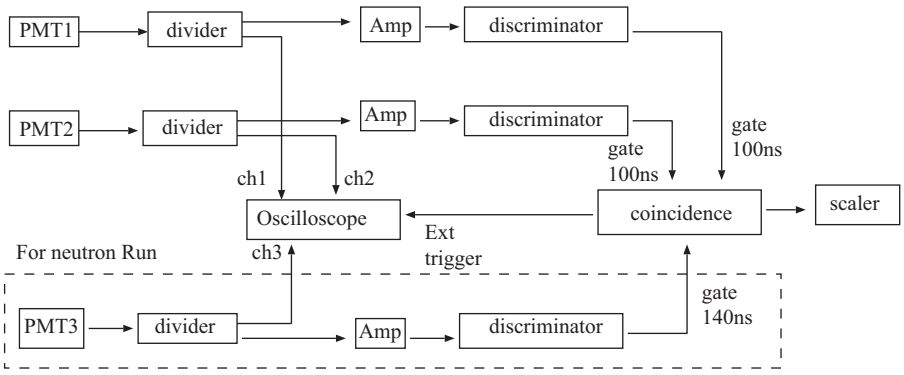

Fig. 2. A schematic diagram of the data acquisition system.

0.58 kg LXe target from the top and bottom respectively. The sides of the target are defined by a highly reflective PTFE surface. Embedded in the PTFE reflector were a LED and a 300 Bq ^{57}Co source. The LED was used to obtain single p.e. spectra and the source to monitor the PMT gain. The light yield from this source was found to be stable within 2%. To protect the LXe from radioactive contamination this ^{57}Co source was enclosed in a thin stainless steel container. The PMTs, the LXe, and the calibration light sources described above were all kept at -100 ± 2 °C inside a stainless steel vessel that itself was suspended inside a vacuum chamber for thermal insulation. Radioactive sources placed outside of the LXe volume and its vacuum enclosure produced the recoil events used in this study: either a ^{137}Cs source provided gamma rays that produced electron events or a gamma tagged ^{252}Cf fission source provided neutrons to study nuclear recoils. To tag the fission events a plastic scintillator and a PMT (labeled PMT3 in Fig. 1) were set up next to the Cf source. In the direction of the LXe on the other hand the gamma rays emitted in the ^{252}Cf fission events were shielded by 50 mm of lead. When filling the setup with LXe the Xe gas was passed through a SAES getter (Model PS4-MT3-R-1) to remove impurities in the Xe gas.

For data acquisition we used NIM logic to trigger recording of the waveform in a LeCroy WavePro 900 digital oscilloscope. This is shown schematically in Fig. 2. Events in the LXe volume were identified by a coincidence of signals in the two PMTs that view the LXe volume. The width of the coincidence timing window is 100 ns, and the discriminator thresholds were set to 2 p.e. equivalent for each PMT. As mentioned above a plastic scintillator was used to tag ^{252}Cf fission events every time the Cf source was employed to produce neutron events in the LXe. The corresponding signal from PMT3 was also entered into the coincidence unit, but with 140 ns gate.

The digital oscilloscope provided 8 bit resolution and a 1 GHz sampling rate. We used it to record 10 μs traces of all PMT signals involved in the respective measurement with 1 ns timing resolution.

The gains of the two PMTs reading out the LXe volume were both set to 3.8×10^6 at the operating temperature of -100 °C, with the HV for PMT1 and PMT2 fixed at 1.26 kV and 1.21 kV, respectively. The single p.e. calibration was obtained from the LED data. The scintillation light yield was then determined to be 20.9 p.e./keV$_{ee}$ from the ^{57}Co spectrum shown in Fig. 3. The energy resolution was 5.4% (RMS) at 122 keV$_{ee}$.

To quantify the impact of the ensuing loss in statistical power on our discrimination method we artificially reduced the light collection in our setup by covering part of the photocathode area of the bottom PMT (PMT2) with a copper mask. While the PMT1 signal was no longer used to estimate the deposited energy in our study with reduced effective light yield, its signal was used in the trigger during that study in the same way as before.

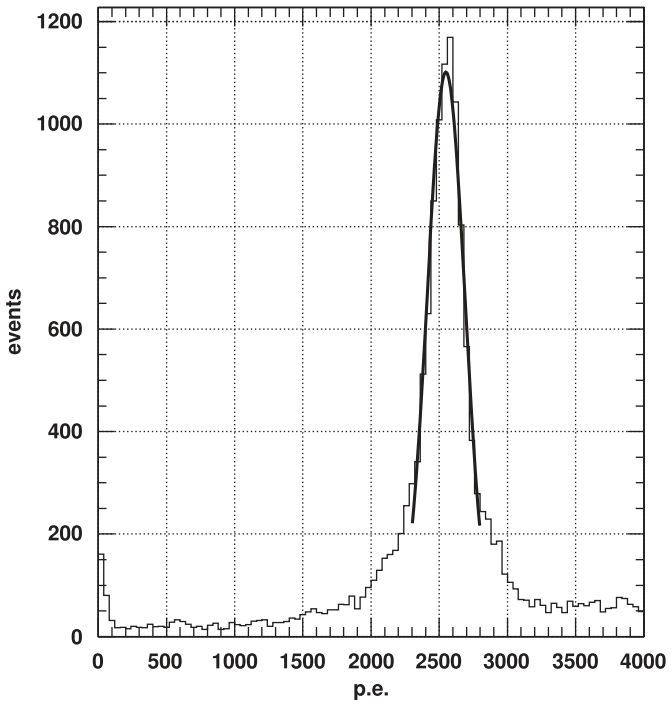

Fig. 3. The p.e. distribution of ^{57}Co data (122 keV gamma-rays) obtained from the sum of the PMT1 and PMT2. The energy resolution was 5.4%.

The resulting ^{57}Co spectrum is shown in Fig. 4, using the p.e. count of only the masked bottom PMT. The effective light yield was thus reduced to 4.6 p.e./keV$_{ee}$ and the energy resolution to 11.7% (RMS) at 122 keV$_{ee}$.

3. Data reduction

A trigger offset of 260 ns allowed us to monitor the baselines 260 ns prior to the recording of our physics events. To ensure the quality of the data sample for both our electron and nuclear recoil event samples we require that none of the events show any "pre-activity" in the first 150 ns from the beginning of its PMT traces, i.e. from 260 ns to 110 ns prior to the event trigger time.

The dynamic range of the oscilloscope was chosen to saturate at a signal height of -400 mV for the PMTs that read out our LXe volume. To avoid problems with saturation, we disregard events where PMT traces from either PMT1 or PMT2 dropped below -350 mV, which is roughly equivalent to 1000 p.e. for electron events.

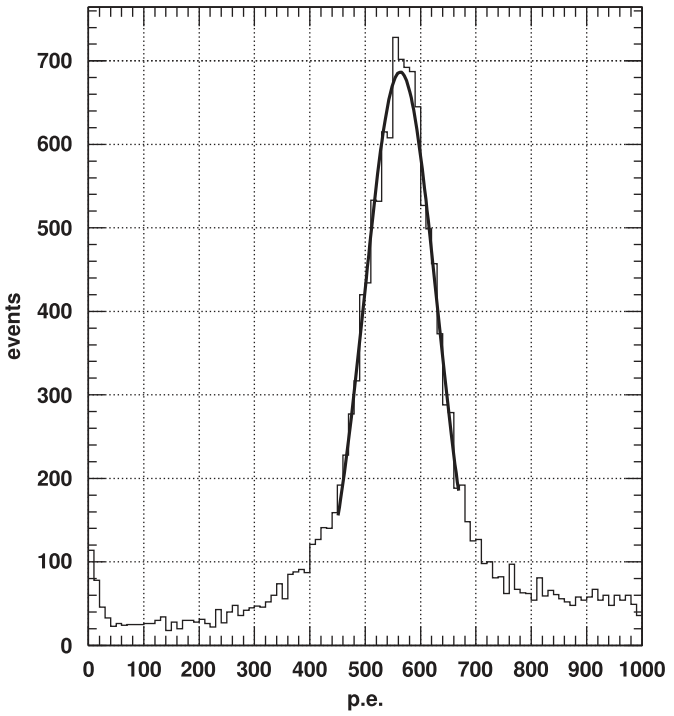

Fig. 4. The p.e. distribution of ^{57}Co data obtained from the masked PMT2 only. The light yield was reduced to 4.6 p.e./keV$_{ee}$ by that mask. The energy resolution was 11.7%.

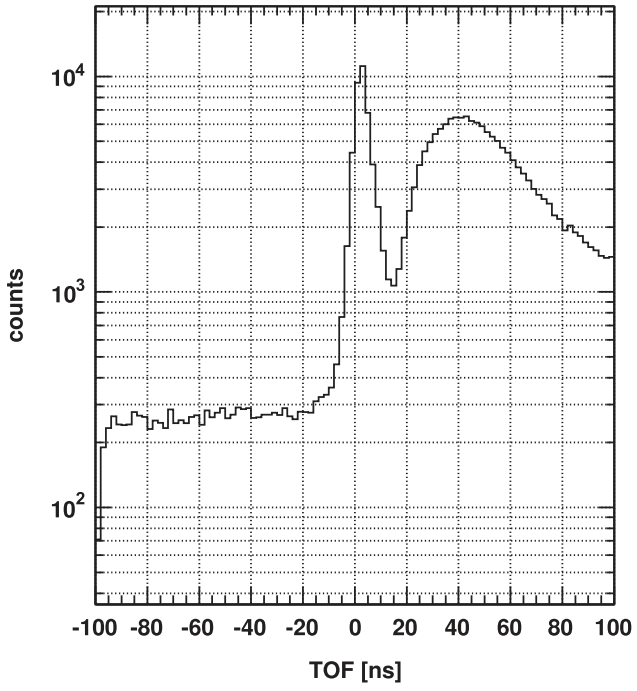

Fig. 5. TOF distribution of ^{252}Cf Run.

Neutron events are identified by the neutron's time of flight (TOF) in the offline analysis. Fig. 5 shows the TOF distribution extracted from software threshold crossings between the leading edges of PMT3 and PMT2. The software thresholds for all timing determinations corresponds to the typical height of a 3 p.e. signal from the PMTs. The peak at zero timing is due to ^{252}Cf fission gammas passing through the lead shielding. To limit the gamma ray background in the sample and specifically select fast neutrons a narrow TOF range from 15 ns to 30 ns was chosen for further analysis.

Table 1 summarizes our data reduction.

Table 1
Data reduction summary of PSD measurement. The number of events before and after each step in the event selection are shown.

	^{252}Cf (neutron) Run	^{137}Cs (gamma ray) Run
Before cuts	8.0×10^5	4.0×10^5
After pre-activity cut	5.6×10^5 (69%)	3.5×10^5 (88%)
After saturation cut	2.2×10^5 (27%)	7.4×10^4 (18%)
After TOF selection	2.2×10^4 (2.7%)	

4. Pulse shape discrimination

The parameter we chose to discriminate between electron and nuclear recoil events is the ratio R_{PSD} as defined in Eq. (3). This ratio is determined by the prompt scintillation light detected in just the first $\Delta t_{t1}=20$ ns and the total amount of scintillation light detected in that same pulse. As we measure light with PMTs, the amounts of prompt and total light are recorded in units of p.e.: $p.e._{.prmt}$ and $p.e._{.tot}$. The window for evaluating the amount of total light starts at the same time t_0 as that for the prompt light and is $\Delta t_{tot}=200$ ns long. t_0 is the same software threshold crossing time as used in the TOF distribution (Fig. 5). Therefore each PMT has its own software threshold crossing resulting in potentially slightly different start times t_{01} and t_{02} for the integration of a PMT's respective scintillation signal. While in our case the size of the setup rendered TOF corrections irrelevant and the scope trace encoded the arrival times of many photons, realistic large volume detectors would have to calibrate timing offsets between many PMTs and apply proper TOF subtraction to obtain viable results. Our respective integrals for prompt and total charges measured from the base line subtracted oscilloscope traces $V_{PMT1}(t)$ and $V_{PMT2}(t)$ of the scintillation signal recorded by PMT1 and PMT2 respectively are added as the ratio is evaluated for each event:

$$R_{PSD}=\frac{\int_{t_{01}}^{t_{01}+\Delta t_{t1}} V_{PMT1}\,dt+\int_{t_{02}}^{t_{02}+\Delta t_{t1}} V_{PMT2}\,dt}{\int_{t_{01}}^{t_{01}+\Delta t_{tot}} V_{PMT1}\,dt+\int_{t_{02}}^{t_{02}+\Delta t_{tot}} V_{PMT2}\,dt}=\frac{p.e._{.prmt}}{p.e._{.tot}}. \quad (3)$$

The 20 ns width for the prompt timing window was optimized for best discrimination against electron events. In the case of the reduced effective light yield measurement all terms involving V_{PMT2} are simply dropped. A possible systematic effect from recoil event positions in the LXe volume was studied with the help of the light balance in the two PMTs.

4.1. Neutron data

The recoil energy E_r of a xenon nucleus elastically scattered on by a neutron with energy E_n is expressed by the following equation:

$$\frac{E_r=E_n 2(A+1-\cos^2\theta-\cos\theta\sqrt{A^2-1+\cos^2\theta})}{(1+A)^2} \quad (4)$$

where A is the mass number of the recoil nucleus, and θ is the scattering angle of the neutron. The maximum recoil energy at $\theta\sim180^\circ$ is 220 keV$_r$ for an 8 MeV neutron. To estimate the light yield we need to know the relative scintillation efficiency L_{eff} that describes the scintillation light yield of a nuclear recoil event as compared to the yield of an electron event at the same energy; we assume $L_{eff}=0.2$ [9]. With that the maximum visible energy for a

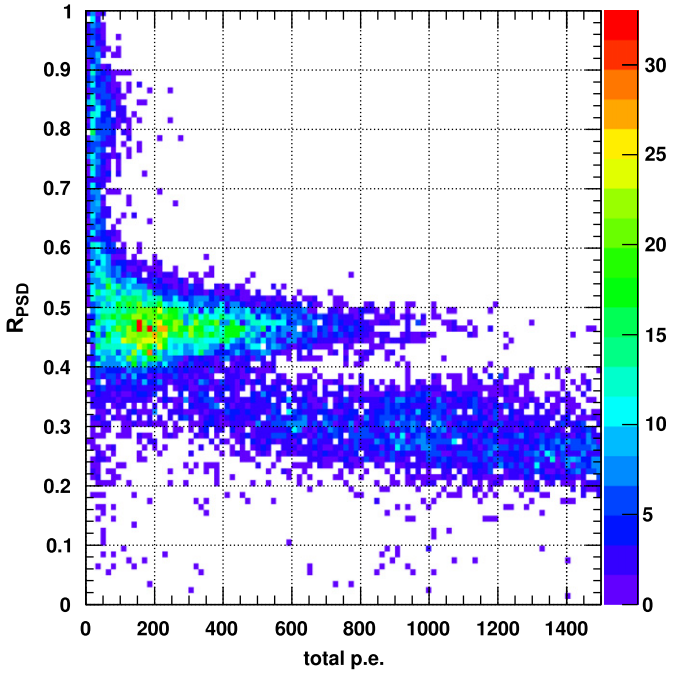

Fig. 6. The scatter plot between total p.e. and R_{PSD} for TOF from 15 to 30 ns in the ^{252}Cf data.

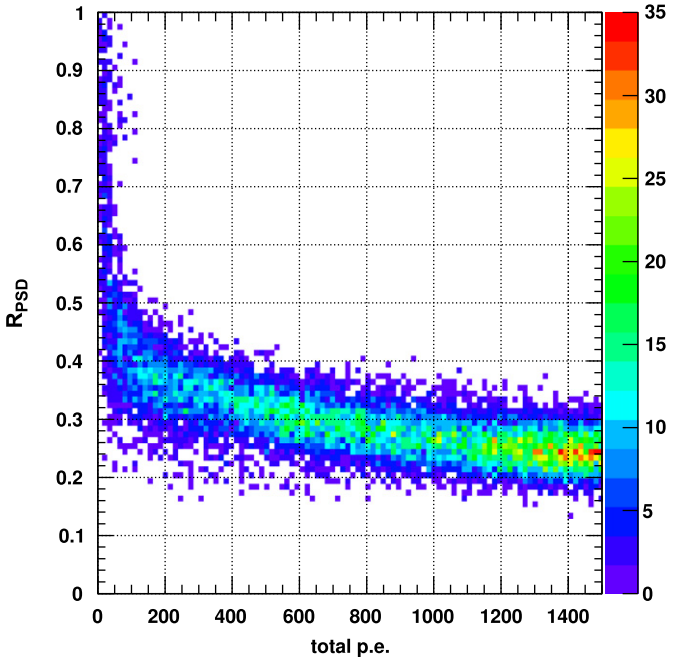

Fig. 7. The ^{137}Cs scatter plot between total p.e. and R_{PSD}.

Xe nucleus recoiling in LXe from the elastic scattering of an 8 MeV neutron is 44 keV$_{ee}$, corresponding to about 920 p.e. in our setup.

The trigger rate for the neutron data run with the ^{252}Cf source was 13.2 Hz (coincidence rate of PMT1&PMT2&PMT3). The trigger rate of PMT3 alone was 16.2 kHz and the coincidence of just PMT1 and PMT2 occurred at 1.12 kHz.

Accidental coincidences in the sample can be estimated from the background in the TOF distributions for each energy range individually, and are found to be less than 5% after our event selection.

Fig. 6 shows the correlation between total p.e. and R_{PSD} for the neutron data. The nuclear recoil band just below $R_{PSD}=0.5$ can clearly be seen, ending about where expected from the above calculation of maximal recoil energy. At higher p.e. we also find gamma rays caused by inelastic scattering below $R_{PSD}=0.4$, which is well separated from the nuclear recoils. The cluster at high $R_{PSD}\sim 0.8$ was caused by very sharp pulses such as Cherenkov light generated in the PMT window.

4.2. Gamma-ray data

Gamma ray data were taken with an external ^{137}Cs source and a lead collimator for the source. The trigger rate of the ^{137}Cs Run was 4.52 kHz (PMT1&PMT2). Fig. 7 shows the correlation between total p.e. and R_{PSD} for this electron event sample. While the average R_{PSD} was rather constant for nuclear recoils in the ^{252}Cf data down to low energies, it does increase for gamma-rays at low energies, slowly merging into the nuclear recoil region as recoil energies approach zero.

5. Results

From Figs. 6 and 7 we expect that the power of R_{PSD} to isolate nuclear recoils and reject gamma-ray background is a function of the scintillation light output observed in our recoil event. To estimate the rejection power for gamma-ray background as a function of energy from our data we proceed in three steps: First we split our data sample into energy bands according to the total p.e. count observed with both, PMT1 and PMT2. We then fit Gaussian distributions to both of the R_{PSD} distributions, the one for nuclear recoils and the one for electron events, separately in each energy band. In the third step we estimate the contamination in the nuclear recoil sample from the tail of the gamma-ray Gaussian that extends beyond the mean of the nuclear recoil Gaussian. Integrating the tail of the fitted distribution beyond the other distribution's mean was compared to straightforwardly counting events in the region integrated over. Counting events was found to give the same result. We define the fractional electron leakage r_{EL} into our nuclear recoil sample at an efficiency of 50% for nuclear recoils:

$$r_{EL}=\int_{\mu_n}^{+\inf} G_e\,dx. \tag{5}$$

Here G_e denotes the normalized Gaussian as fitted to the R_{PSD} distribution for electron events, which has a mean μ_e and a variance σ_e. G_n, μ_n, and σ_n stand for the corresponding entities derived from the fit to the R_{PSD} distribution of the nuclear recoils.

Fractional electron leakage was evaluated for the p.e. ranges of 100–150, 150–200, 200–250, 250–300, and 300–400 p.e. Using a conversion factor of 20.9 p.e./keV$_{ee}$, these p.e. ranges correspond to energy ranges of 4.8–7.2, 7.2–9.6, 9.6–12, 12–14.4, and 14.4–19.1 keV$_{ee}$ respectively. We approximated the energy scale assuming that the scintillation light yield is linear in energy. Fig. 8 shows the R_{PSD} distributions for both the nuclear and the electron event samples in the energy range from 4.8 to 7.2 keV$_{ee}$. The corresponding Gaussian fits are also shown.

Fig. 9 summarizes the fractional electron leakages we measured in the energy ranges listed above. Horizontal bars reflect the range of electron equivalent recoil energy that was used. Vertical error bars show the statistical uncertainties; the range between the braces has the systematic uncertainties added quadratically. The largest contribution to the systematic uncertainty came from the single p.e. determination. Open circles show the results for the study with the artificially reduced effective light yield of 4.6 p.e./keV$_{ee}$, while solid

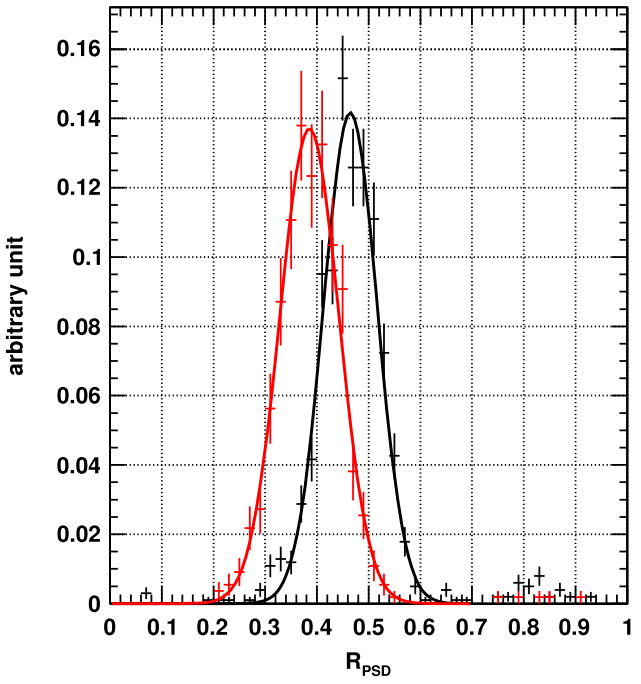

Fig. 8. The R_{PSD} distribution in the energy range between 4.8 and 7.2 keV$_{ee}$. The red and black lines show the ^{137}Cs data and the ^{252}Cf data, respectively. (For interpretation of the references to color in this figure legend, the reader is referred to the web version of this article.)

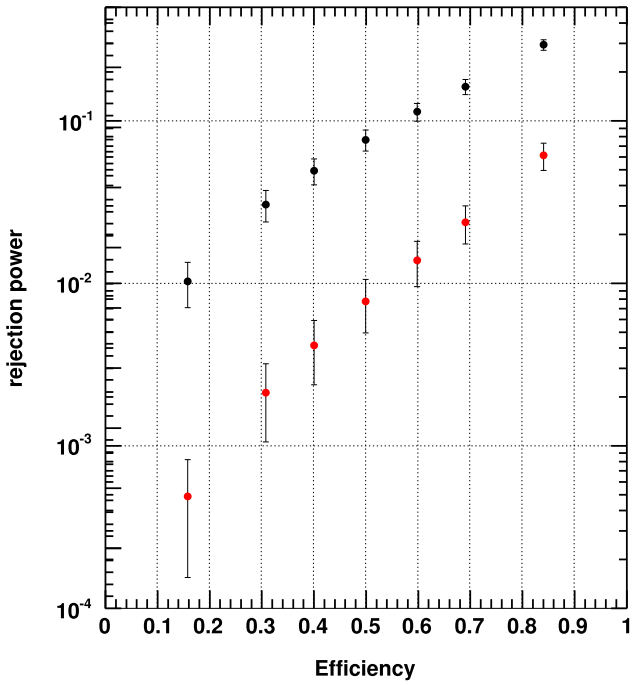

Fig. 10. The efficiency dependence of nuclear recoil retention on rejection power. The black and red points show the rejection power in the energy range 4.8–7.2 keV$_{ee}$ and 9.6–12 keV$_{ee}$ for non-masked data, respectively.

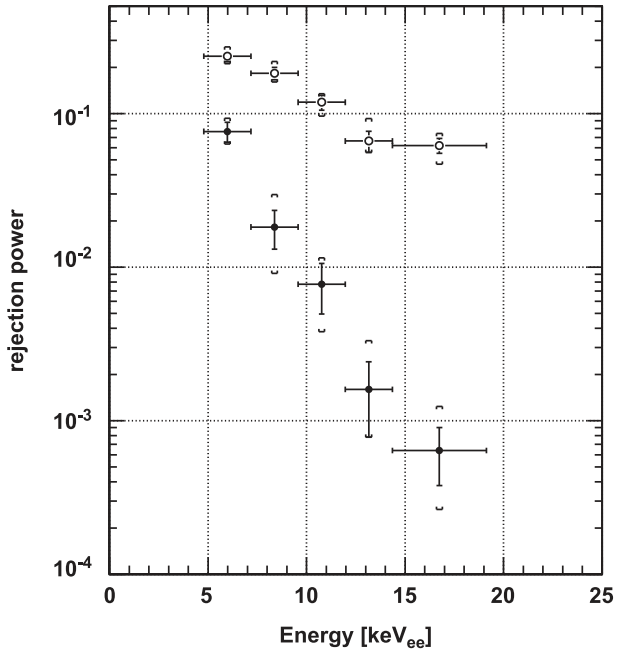

Fig. 9. The rejection power distribution. The open and filled circle points show the masked (4.6 p.e./keV) and non-masked (20.9 p.e./keV) data. Error bars shows the statistical error. Braces show the error including systematic uncertainty added in quadrature.

circles show the rejection power for the full measured scintillation light yield of 20.9 p.e./keV$_{ee}$.

So far we discussed electron recoil rejection at a fixed efficiency for nuclear recoil events of 50%. Fig. 10 shows how efficiency and rejection trade off against each other for non-masked data in the energy ranges 4.8–7.2 keV$_{ee}$ and 9.6–12 keV$_{ee}$.

6. Discussion

Our study clearly shows that PSD can be used in pure scintillation based LXe dark matter detectors. As expected its power depends on the effective light yield. Our r_{EL} measure as defined above ultimately depends on the relative size of two quantities: the distance of the two means $\mu_n-\mu_e$ as compared to the width of the electron distribution σ_e.

In Fig. 11 we compare the mean values of the R_{PSD} distributions for the electron and nuclear recoil runs as a function of our energy ranges. Both the high yield data and the data taken with an artificially lower effective yield are shown, and it can be seen that the means change by less than 5% as we change the light yield.

The effect of this systematic change in $\mu_n-\mu_e$ contributes only 4% to the overall efficiency loss; the larger contribution comes from the widening of the distribution.

Looking at the electron distribution width σ_e, we tried to separate the statistical component reflecting the p.e. statistics from an intrinsic component reflecting the physics of the various processes involved in generating, detecting, conditioning, and recording the signal. Figs. 12 and 13 respectively show σ_e and σ_n, again as a function of our energy ranges.

To estimate the statistical contribution to the width of the R_{PSD} we used a Monte Carlo (MC) simulation. In this process we first randomly chose a value for $p.e._{tot}$ in the relevant range from 50 to 400 p.e. Using the fits to our R_{PSD} means as shown in Fig. 14 we determine the proper R_{PSD} mean to use for this $p.e._{tot}$ value. Using $p.e._{tot}$ and its proper R_{PSD}, the MC obtains a set of $p.e._{prmt}$ by sampling from the binomial distribution:

$$P(p.e._{prmt}) = {}_{p.e.tot}C_{p.e._{prmt}\cdot tot} R_{PSD}^{p.e._{prmt}}(1-R_{PSD})^{p.e._{tot}-p.e._{prmt}} \quad (6)$$

where C represents the appropriate binominal coefficient. From this set of $p.e._{prmt,MC}$ we calculate a set of $R_{PSD,MC} = p.e._{prmt,MC}/p.e._{tot}$.

$R_{PSD,MC}$ distributions are built up for both the electron and nuclear recoil means and fitted to Gaussians to extract $\mu_{e,MC}$,

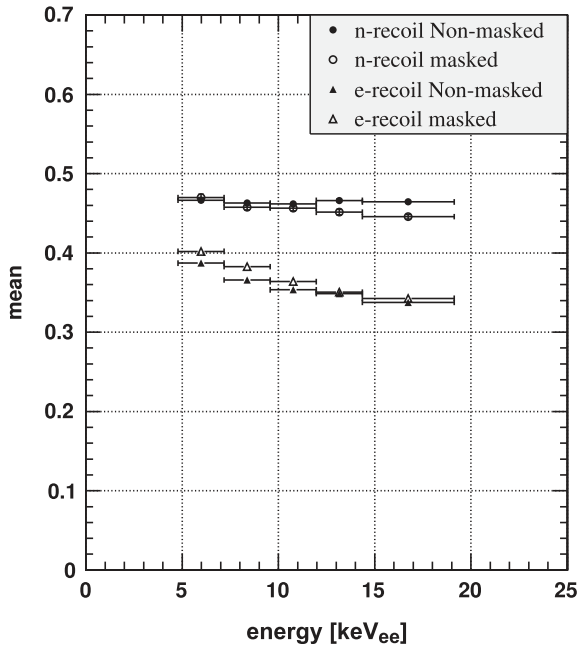

Fig. 11. Mean value of the R_{PSD} as a function of observed energy in units of keV$_{ee}$ for ^{137}Cs runs and ^{252}Cf runs. The filled and open triangle points show the values of ^{137}Cs runs for the non-masked PMT1+PMT2 (20.9 p.e./keV) and for the masked PMT2 (4.6 p.e./keV), respectively. The filled and open circle points show the values of ^{252}Cf data for the non-masked PMT1+PMT2 (20.9 p.e./keV) and for the masked PMT2 (4.6 p.e./keV), respectively.

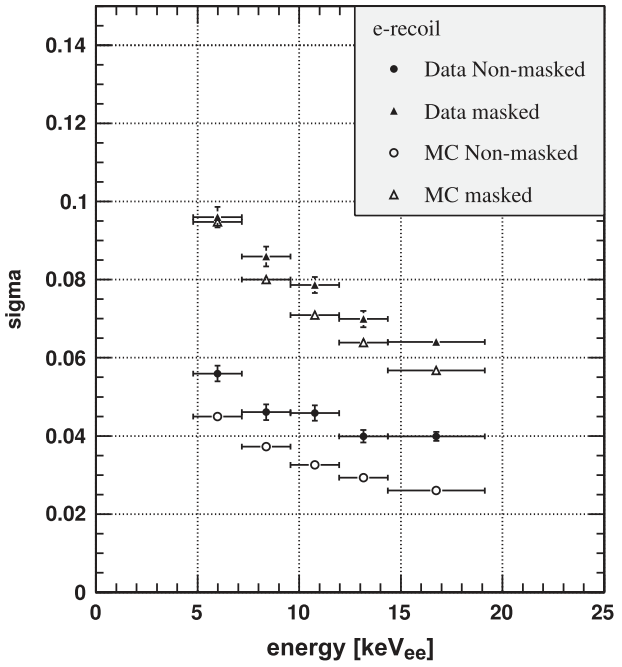

Fig. 12. Sigma of the R_{PSD} distribution as a function of observed energy in units of keV$_{ee}$ for ^{137}Cs data. The filled circle and filled triangle points show the values for the non-masked PMT1+PMT2 data (20.9 p.e./keV) and for the masked PMT2 data (4.6 p.e./keV), respectively. The open circle and open triangle points show the MC simulation of the non-masked PMT1+PMT2 (20.9 p.e./keV) and the masked PMT2 (light yield was reduced to 4.6 p.e./keV), respectively.

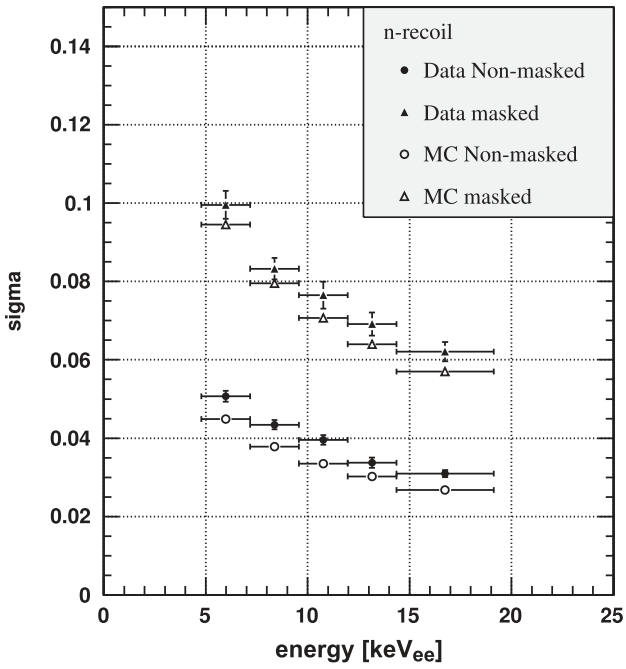

Fig. 13. Sigma of the R_{PSD} distribution as a function of observed energy in unit of keV$_{ee}$ for ^{252}Cf data. The filled circle and filled triangle points show the values for the non-masked PMT1+PMT2 (20.9 p.e./keV) and for the masked PMT2 (4.6 p.e./keV), respectively. The open circle and open triangle points shows the MC simulation of the non-masked PMT1+PMT2 (20.9 p.e./keV) and the masked PMT2 (light yield was 4.6 p.e./keV).

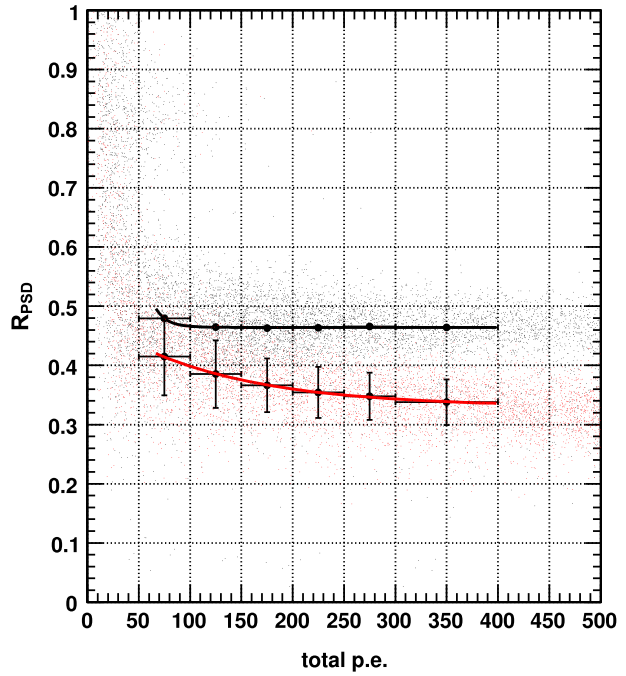

Fig. 14. The relation between R_{PSD} and total p.e. The black and red lines show the fit function of ^{252}Cf and ^{137}Cs. The error bars of ^{137}Cs represent the width (1σ) of the distribution. For reference we underlay the fit functions with the ^{252}Cf (black dots) and ^{137}Cs (red dots) data. (For interpretation of the references to color in this figure legend, the reader is referred to the web version of this article.)

$\sigma_{e,MC}$, $\mu_{n,MC}$ and $\sigma_{n,MC}$. The resulting $\mu_{e,MC}$ and $\mu_{n,MC}$ are in good agreement with their measured counterparts μ_e and μ_n.

Figs. 12 and 13 show the variances of σ for MC and data compared for electron and nuclear recoil respectively. Systematically the MC data are less spread than the real data, but the effect is quite striking for the high light yield electron event data.

In the case of electron events the waveform is dominated by recombination, which is slow. In case of nuclear recoil, the waveform reflects the relatively short lifetimes of the singlet and triplet

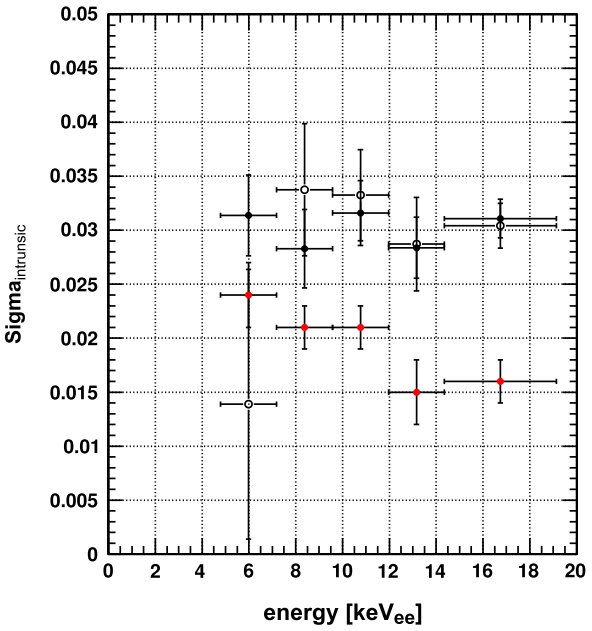

Fig. 15. The $\sigma_{intrinsic}$ distribution of electron events and nuclear recoil events. The black open and filled circle points show the values of the masked and the non-masked data, respectively. The red points show the $\sigma_{intrinsic}$ distribution of nuclear recoil events of the non-masked data. (For interpretation of the references to color in this figure legend, the reader is referred to the web version of this article.)

states. Fluctuations in the energy deposit along the electron track will translate into fluctuations in the recombination time scale and might be one mechanism by which additional fluctuations can propagate into our R_{PSD} parameter. In an effort to quantify the extra contribution $\sigma_{intrinsic}$ to the width of our distribution that is evident in our data we calculated:

$$\sigma_{intrinsic} = \sqrt{\sigma^2_{data} - \sigma^2_{MC}}. \quad (7)$$

In case of electron events, the high and low light yield data are consistent as shown in Fig. 15, which is expected if the intrinsic width reflects processes associated with the production of the scintillation light. In both cases the same amount of light is actually produced, but only a fraction of it is used in the masked case. In the energy range that we investigated the intrinsic contribution to the electron width does not depend on energy. In case of nuclear recoil events, the $\sigma_{intrinsic}$ is smaller than electron events as shown in Fig. 15.

7. Conclusion

PSD in liquid xenon was studied at energies relevant to dark matter searches. A significant difference in pulse shape between nuclear recoil and electron events was exploited in a high light yield setup in which 5 keV_{ee} of deposited energy produced 100 p.e. equivalent in PMT signal output.

At high light yield (20.9 p.e./keV_{ee}) our R_{PSD} parameter allows a rejection of electron events by a factor of $7.7 \pm 1.1(\text{stat}) \pm {}^{1.2}_{0.6}(\text{sys}) \times 10^{-2}$ in the energy range between 4.8 and 7.2 keV_{ee} with a 50% efficiency to retain nuclear recoil events. In the energy range 14.4–19.1 keV_{ee} electron events were reduced by more than three orders of magnitude with the same efficiency for nuclear recoils.

The dependence of this rejection power on photon statistics was also studied. At low effective light yield (4.6 p.e./keV_{ee}), a rejection of electron events by a factor of $2.4 \pm 0.2(\text{stat}) \pm {}^{0.3}_{0.2}(\text{sys}) \times 10^{-1}$ was demonstrated for the energy range 4.8–7.2 keV_{ee} with a 50% efficiency for nuclear recoil events.

In our MC replication of the experimental results the width of the R_{PSD} distribution for nuclear recoils is almost exhausted by the expected purely statistical contribution to that width, while that is clearly not the case for electron events. This excess width is tentatively interpreted as stemming from fluctuations inherent to the energy deposition of electron events.

Acknowledgements

We gratefully acknowledge the cooperation of Kamioka Mining and Smelting Company. This work was supported by the Japanese Ministry of Education, Culture, Sports, Science and Technology, and Grant-in-Aid for Scientific Research. We are supported by Japan Society for the Promotion of Science.

References

[1] K.G. Begeman, A.H. Broeils, R.H. Sanders, Monthly Notices of the Royal Astronomical Society 249 (1991) 523.
[2] J. Dunkley, et al., Astrophysical Journal Supplement 180 (2009) 306.
[3] R.A. Knop, et al., Astrophysical Journal 598 (2003) 102.
[4] A.W. Allen, et al., Monthly Notices of the Royal Astronomical Society 334 (2002) L11.
[5] M. Tegmark, et al., Physical Review D 69 (2004) 103501.
[6] G. Jungman, et al., Physics Reports 267 (1996) 195.
[7] R. Bernabei, et al., European Physical Journal C 56 (2008) 56.
[8] Z. Ahmed, et al., Science 327 (2010) 1619.
[9] E. Aprile, et al., Physical Review Letters 105 (2010) 131302.
[10] Y. Suzuki 〈arXiv:0008296〉.
[11] S. Kubota, et al., Journal of Physics 11 (1978) 2645.
[12] S. Kubota, et al., Physical Review B 20 (1979) 3486.
[13] A. Hitachi, T. Takahashi, Physical Review B 27 (1983) 5279.
[14] A. Hitachi, Astroparticle Physics 24 (2005) 247.
[15] E. Aprile, T. Doke, Reviews of Modern Physics 82 (2010) 2053.
[16] E. Aprile, et al., Physical Review Letters 97 (2006) 081302.
[17] R. Bernabei, et al., Physics Letters B 436 (1998) 379.
[18] G.J. Alner, et al., Astroparticle Physics 23 (2005) 444.
[19] J. Kwong, et al., Nuclear Instruments and Methods in Physics Research Section A 612 (2010) 328.